Steel and Composite Structures, *Vol. 57, No. 3 (2025) 261-274*
https://doi.org/10.12989/scs.2025.57.3.261

Analysis of tubular structures subjected to extreme loading and corrosion/repair processes

Scarlet K. Montilla*[1], Yongtao Bai[1], JiePeng Liu[1], Ricardo Picón[2], Néstor Guerrero[3], Mohamed Elchalakani[4] and Julio Flórez-López[1]

[1]School of Civil Engineering, Chongqing University, 400045, Chongqing, China
[2]Catholic University of Temuco. Department of Civil Engineering and Geology, Chile
[3]Department of Civil Engineering, University of Ibagué, Ibagué, Colombia
[4]Civil Engineering School, The University of Western Australia, WA 6009, Perth, Australia

(Received November 22, 2023, Revised August 2, 2025, Accepted September 11, 2025)

Abstract. Complex tubular structures are often exposed to aggressive environments that produce corrosion and, occasionally, must be able to withstand extreme mechanical overloads. Thus, health monitoring, computational simulation tools, and repair projects are critically required to assure the fulfillment of the expected service life. A very important retrofitting technique consists of the use of carbon fiber-reinforced polymers. This paper proposes a new multi-scale formulation that describes the coupling of corrosion/repair processes with plasticity and local buckling effects, specifically adapted for the analysis of complex structures. A lumped damage model is proposed that includes corrosion laws in the constitutive equations. Coupling between corrosion, repair, plasticity and local buckling is carried out by extended "interaction diagrams". Repair is characterized as a "negative corrosion increment". The structural assessment is carried out by the introduction of a "damage driving rotation" that determines the closeness of local buckling during cyclic loadings. Collapse risks are evaluated by using a local buckling state variable. This new model is implemented as a finite element in which corrosion is a nodal degree of freedom. This computational tool can be used for the design of deterministic or reliability-based management of inspection, maintenance, or repair of offshore and other complex tubular structures.

Keywords: complex networks; mathematical simulation; mechanical behavior; nanotechnology

1. Introduction

Tubular elements are the basis of many types of complex structures, especially in offshore engineering, civil construction, and nuclear facilities. Often, these steel members need repairs during their service life. Repairing may be required due to corrosion, impacts, earthquakes, or other unexpected extreme loadings.

A very effective repair technique consists of the use of CFRP composites on onshore structures (Meiling and Sreekanta 2009, Elchalakani and Fernando 2012, Uriayer and Alam 2013, Elchalakani 2014, Elchalakani *et al.* 2017, Hamzeh 2017, Aksoylu *et al.* 2023) as well as offshore ones (Momber 2011, George *et al.* 2021, George *et al.* 2022a).The effect of the number of layers on the strength of elements has already been established (Bambach *et al.* 2009, Kabir *et al.* 2015). Corrosion may be due to many different causes: the presence of water or moisture and oxygen, friction and wear, surface contamination, and so on (Jabed *et al.* 2023). Thus, the modeling of corrosion presents very different laws that depend on completely dissimilar driving forces.

The numerical models for corrosion may be divided into two groups, heuristic and deterministic. The heuristic models are obtained from the regression of measured data, e.g., weight loss measurements or corrosion rate as a function of varied environmental parameters. Deterministic approaches are multi-scale models that account for the fundamentals of corrosion mechanisms to simulate the corrosion rate (Di Sarno *et al.* 2021). The former group is of special interest in the procedures proposed in this paper.

A corrosion law for the conditions of structures in rivers was proposed by Liu *et al.* (2022), its driving corrosion variables are the flow velocity and sediment concentration (Lee *et al.* 2015). In marine conditions, many heuristic corrosion laws have been proposed, a partial list of them can be found in (Di Sarno *et al.* 2021). Corrosion may depend on SO2 concentration, relative humidity, time of wetness, or air salinity (Rahgozar *et al.* 2010, Kainuma *et al.* 2018)

Extreme mechanical loadings on tubular structures may generate two main types of inelastic effects: plasticity and local buckling. The approaches for their modeling can be grouped into three categories, nonlinear shell theories (Chakrabarty 2006, Amabili, 2008), moment-curvature constitutive laws (Sohal and Chen 1984) and lumped damage models (Inglessis *et al.* 1999, Febres *et al.* 2003, (Inglessis *et al.* 2002). For complex structures, the last approach is particularly effective, combining computational economy with good engineering precision for reliability analyses (Kim and Noh 2012, (Palanisamy *et al.* 2019,

*Corresponding author, Ph.D. Student
E-mail: scarlet.kmb03@gmail.com

http://www.techno-press.com/journals/scs&subpage=8 ISSN: 1229-9367 (Print), 1598-6233 (Online)

Djeddi and Amirat, 2020). It has been shown that lumped damage models are especially well-adapted for probabilistic structural analyses (Coelho *et al*. 2019, Bazán *et al*. 2019, Coelho *et al*. 2022) and this property is extremely important for the structural assessment of long time periods given the random nature of the chemo-mechanical loadings involved in the process.

The goal of the present work is the proposal of a multi-scale procedure for the integration of corrosion models and repair strategies into structural analyses. The resulting computational tools may be used for the design or evaluation of repair projects and protocols. It could also be used for the reliability and probabilistic analysis of this kind of structure, although this subject is outside of the scope of the present paper. Another important application is the consideration of in-the-field assessments of corrosion in existing structures and the inclusion of the effects of previous repairing processes.

As the subject is the analysis of complex structures, the framework considered is that of lumped damage models. A particularity of the problem is that the characteristics of the structure (stiffness, strength, etc.) cannot be considered constants but evolve over time. Thus, a lumped model is generalized by the inclusion of the corrosion laws in the constitutive equations. Coupling between corrosion, repair, plasticity and local buckling is carried out by extended "interaction diagrams"; repair is characterized as a "negative corrosion increment" The structural assessment is carried out by the introduction of a "damage driving rotation" that determines the closeness of local buckling during cyclic loadings. Collapse risks are evaluated by the use of local buckling state variable.

The numerical implementation of these models proposed in this paper consists of the development of finite elements, where not only displacements, but also corrosion are degrees of freedom and external mechanical as well as corrosion driving variables are nodal forces. These finite elements can be included in any nonlinear structural analysis program, like the well-known ABAQUS or ANSYS. Therefore, if in-the-field measurements of corrosion/repair processes are available, they can be included in the analysis in the same way that imposed displacements and boundary conditions are. If the prediction of future behavior is the goal, then corrosion-driving variables can be imposed in the same way as the histories of external forces.

This paper is organized as follows: In section 2, a brief and not exhaustive review of heuristic corrosion laws is presented. Some experimental results on tubular structures with and without corrosion/repair are described in section 3. The model and its numerical implementation for the particular case of mono-sign loadings are proposed in section 4. The resulting computational tool was used for the simulation of the tests in section 3 and its results are presented in section 5. In section 6, the model is extended to the case of planar frames subjected to general cyclic and earthquake loadings in section 6. Two parametric examples showing potential applications of the new formulation are described in section 7.

2. Some phenomenological (heuristic) corrosion laws

2.1 Corrosion evolution under fluvial conditions

A corrosion law adapted to the specific conditions of the Yangtze River in China, was proposed by Liu *et al*. (2022). It was reported that the evolution over time of the corrosion depth (cor) can be described, with a good fitting correlation, by:

$$cor = a_1 + a_2 \ln(t + a_3) \tag{1}$$

Where parameters a_1, a_2, a_3 depend on the flow velocity and t is the corrosion time.

In addition, the corrosion process reduces the strength of the material. Let th_0 be the original thickness of a tubular element and th the corroded one. A corrosion state variable at a specific location i is defined as:

$$c_i = 1 - \frac{th}{th_0}; \qquad th = th_0 - cor \tag{2}$$

Note that the corrosion state variable is a normalized corrosion depth, taking values into the interval $[0,1]$. Shi *et al*. 2012 proposed an expression describing the reduction of the material's strength as a function of the corrosion state variable:

$$f_u = (1 - 0.98c_i) f_{u0} \tag{3}$$

Where f_u is the steel material strength value at a certain corrosion time t, and f_{u0} is the initial steel strength value.

2.2 Corrosion evolution under fluvial conditions

This short review is based on a report by Klinesmith *et al*. 2007. The simplest corrosion depth law in marine conditions is (Liu *et al*. 2022, ISO-9224, 2012)

$$cor = At^B \tag{4}$$

where A is the first-year corrosion rate, B is the coefficient that shows the long-term exposure effect considering the protective products and environmental factor, and t is again the corrosion time.

Another model establishes differences between the corrosion evolution before and after 20 years of exposure (ISO-9223, ISO-9224, ISO-9226, 2012):

$$cor = \begin{cases} At^B, & t < 20 \\ A[20^B + B(20^B - 1)(t - 20)], & t \geq 20 \end{cases} \tag{5}$$

Albrecht and Hall (2003), proposed a nonlinear time-dependent model that can be utilized in different environmental conditions:

$$cor = cor_\infty \left[1 - e^{-t/\tau_t}\right] \tag{6}$$

where cor_∞ is the long-term thickness of the corroded component and τ_t is the transition time.

Considering the interaction between corrosion protection systems and the environment as pitting corrosion, Klinesmith *et al*. (2007), proposed the following expression:

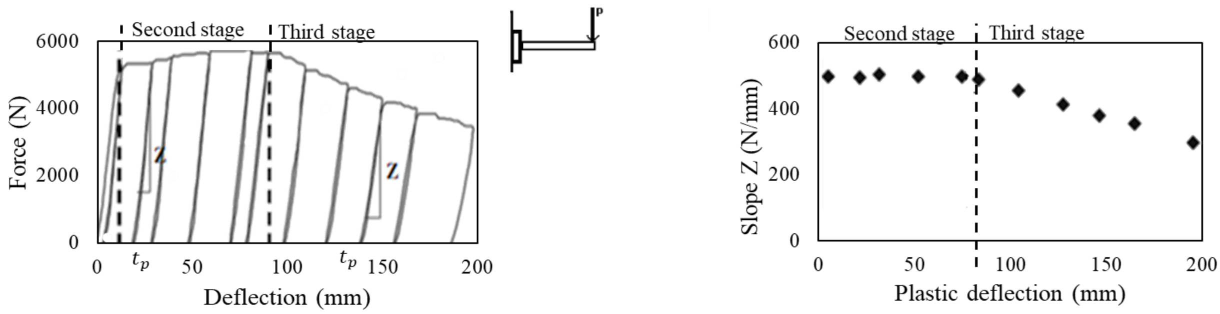

(a) Force vs Deflection (b) Slope vs Plastic Deflection

Fig. 1 The behavior of a cantilevered tubular steel beam subjected to monotonic loading by Febres *et al.* (2003)

(a) Local buckling under cyclic loading (b) Force vs. Deflection test

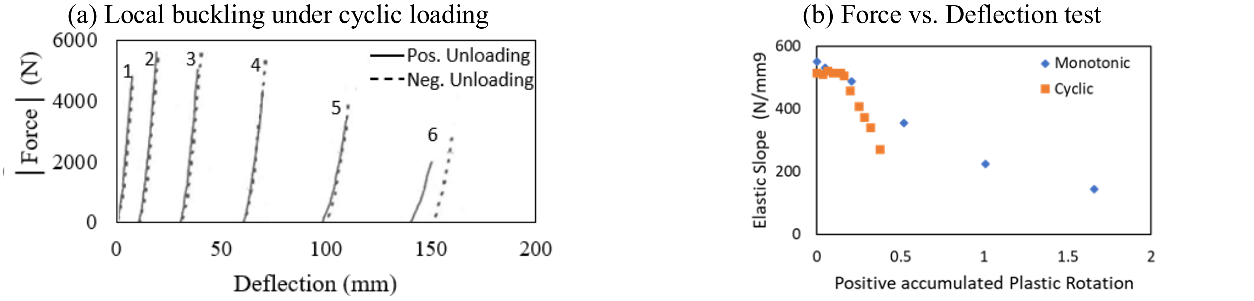

(c) Force vs Displacement during elastic unloading (d) Elastic slope vs. Positive accumulated plastic rotation

Fig. 2 Cyclic tests Febres *et al.* (2003)

$$cor = At^B \left(\frac{TOW}{C}\right)^D \left(1 + \frac{[SO_2]}{E}\right)^F \left(1 + \frac{CL}{G}\right)^H e^{J(T+T_0)} \quad (7)$$

where TOW is annual time of wetness (h/year), T is the air temperature (C), and $A, B, C, D, E, F, G, H, J$ and T_0 are constants.

3. Some experimental results on local buckling

3.1 Mono-sign test in tubular elements

Febres *et al*. (2003) presented the behavior of steel tubes under mono-sign loading (see Fig. 1(a) and 1(b)). Notice the three distinctive stages. The first one can be considered elastic; the second phase corresponds to the appearance of plastic deflections; local buckling initiates the last one, characterized by significant losses of stiffness and strength.

3.2 Cyclic test

Under cyclic tests with positive and negative bending moments (see Fig. 2), distinctive local buckling occurs at both sides in the plastic hinge zone. The behavior in this case can be considered "unilateral"; i.e., the buckling produced by positive bending moments (positive LB) seems to have little effect on the elastic behavior under negative bending moments, and vice versa, as shown in Fig. 2(c).

There is another important effect during cyclic loadings: counter-buckling. This phenomenon can be described as follows: during the positive LB process, a "wrinkle" is formed on the compression side of the tube. When the moment changes sign, this zone becomes subjected to tension stresses; consequently, the "positive wrinkle" is "flattened" under negative bending moments. This "flattening" process does not recover the strength or stiffness of the positive LB but it does slow the progress of buckling at the next cycle, as shown in Fig. 2(d). It can be seen there that local buckling evolves faster, in terms of cumulated plasticity, under mono-sign loadings than cyclic loadings.

3.3 Frame under mono-sign loading

Fig. 3 shows a steel tubular frame with the same square cross-sections for all its elements. The frame was subjected to two horizontal displacement-controlled forces in opposite

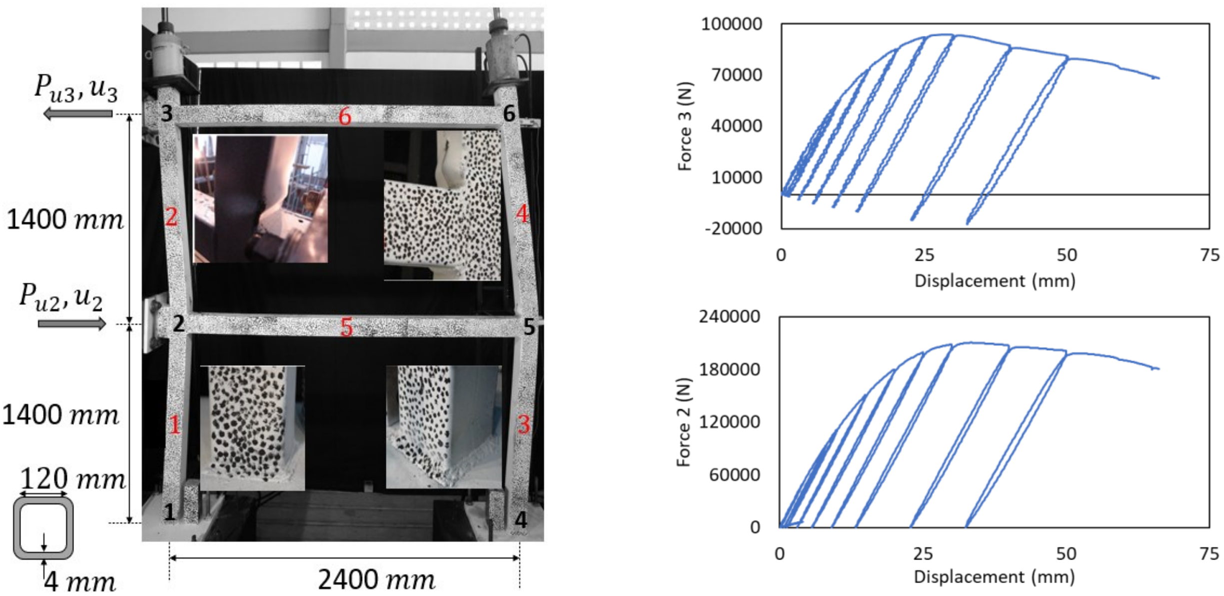

(a) Configuration of the frame (b) Force vs. Displacement

Fig. 3 Tubular steel frame subjected to mono-sign loadings

directions, denoted as p_{u2} and p_{u3}.

The behavior of the frame is represented in the curves of u_2 vs. P_{u2} and u_3 vs. P_{u3}. Local buckling in the columns appeared in the softening phase of the test, as shown in the pictures in the figure.

4. Modeling the coupling of local buckling and corrosion for mono-sign loading

4.1 Corrosion/repairing variable, generalized displacement, and deformation matrices

Consider, for instance, an offshore tubular structure in the plane x, z as the one represented in Fig. 4(a). This frame is divided into m elements connected by n nodes. Consider now an element b between nodes i and j. It is assumed that the element is the assemblage of an elastic beam column and two inelastic hinges as shown in Fig. 4(b). The model proposed by (Febres *et al.* 2003) included only two internal variables per hinge: the plastic rotation ϕ_i^p and a damage parameter characterizing the degree of local buckling: d_i. That model is now extended in order to consider (C/R) processes. The corrosion state variable introduced in section 2 can now take values into the interval $-\infty \leq c_k \leq 1$ (Fig. 4(a)). Notice that c_k might be negative because, during the process of repair, the final strength of the cross-section could have increased beyond the original one. It is also assumed that all the hinges around the same node have the same corrosion level.

As mentioned in the introduction, the goal of the finite element proposed in this section is to include the C/R variable as a degree of freedom. Thus, besides the conventional three degrees of freedom denoted by u_k (displacement in x), w_k (displacement in z) and θ_k (rotation around y), it is added the new variable c_k (Fig. 4(a)). Therefore, the degrees of freedom of the element are grouped into the following generalized displacement matrix: $\{\mathbf{u}\}_b^t = (u_i, w_i, \theta_i, c_i, u_j, w_j, \theta_j, c_j)$.

Another kinematic variable, $\{\mathbf{\Phi}\}^t = (\phi_i^b, \phi_j^b, \delta_b, c_i, c_j)$, called generalized deformation matrix, is introduced; the relative rotations ϕ_i^b, ϕ_j^b and elongation δ_b are represented in Fig. 4(c). Notice that in the deformation matrix, the C/R variables are also included. Displacement and deformation matrices are related by the following kinematic equation:

$$\{\dot{\mathbf{\Phi}}\}_b = [\mathbf{B}]_b \{\dot{\mathbf{u}}\}_b^t$$

$$[\mathbf{B}]_b = \begin{bmatrix} \frac{sin\alpha}{L} & -\frac{cos\alpha}{L} & 1 & 0 & -\frac{sin\alpha}{L} & \frac{cos\alpha}{L} & 0 & 0 \\ \frac{sin\alpha}{L} & -\frac{cos\alpha}{L} & 0 & 0 & -\frac{sin\alpha}{L} & \frac{cos\alpha}{L} & 1 & 0 \\ -cos\alpha & -sin\alpha & 0 & 0 & cos\alpha & sin\alpha & 0 & 0 \\ 0 & 0 & 0 & 1 & 0 & 0 & 0 & 0 \\ 0 & 0 & 0 & 0 & 0 & 0 & 0 & 1 \end{bmatrix} \quad (8)$$

4.2 Nodal force and generalized stress matrices

The conjugated variable to the generalized deformation is called the generalized stress matrix and is defined as: $\{\mathbf{M}\}_b^t = (m_i^b, m_j^b, n_b, p_{ci}, p_{cj})$ where m_i^b and m_j^b are bending moments at, respectively, the ends i and j; n_b is the axial force as shown in Fig 4d. As mentioned in the introduction, another goal of the model is to include phenomenological corrosion laws in the structural analysis of tubular complex structures. Thus, the specific nature of the chemical forces coupled to corrosion (p_{ci}, p_{cj}) depends on the precise law that it is chosen for the analysis. Similarly, the matrix of nodal forces, i.e., the contribution of the element to the matrix of internal forces of the structure, is defined as: $\{\mathbf{P}\}_b^t =$

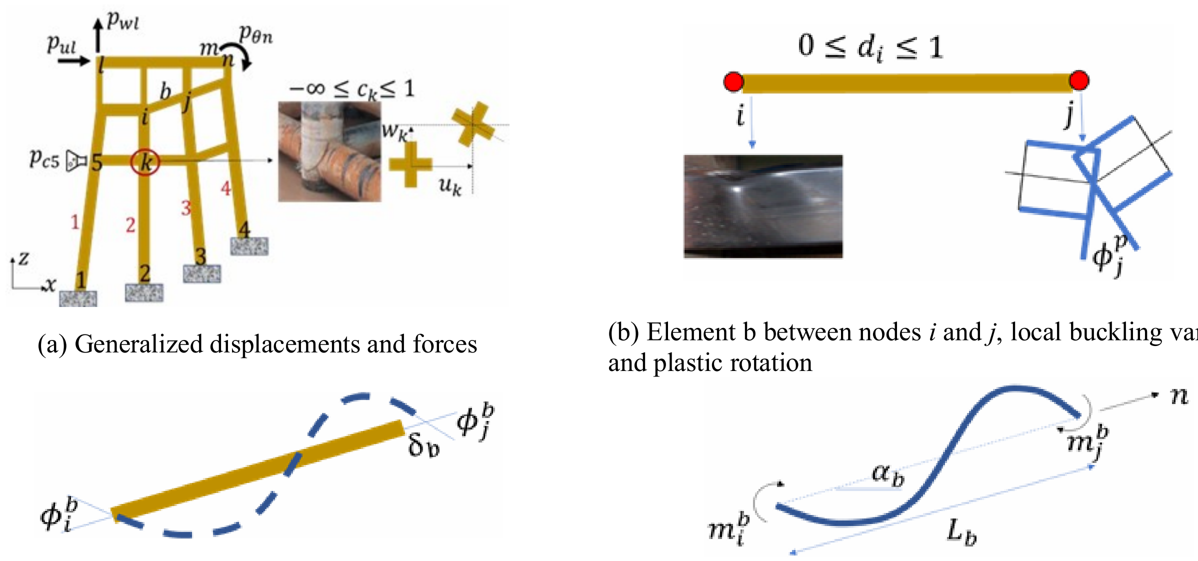

(a) Generalized displacements and forces

(b) Element b between nodes *i* and *j*, local buckling variable and plastic rotation

(c) Generalized deformations

(d) Generalized stresses

Fig. 4 Model configuration of the offshore frame structure

$(p_{ui}, p_{wi}, p_{\theta i}, p_{ci}, p_{uj}, p_{wj}, p_{\theta j}, p_{cj})$; where p_{ui} is the force on the node i in the direction of the axis x. p_{wi} is the force applied on the same node but in the direction of the axis z. Finally, $p_{\theta j}$ is the couple. The relationship between the nodal force and generalized stress matrices is the following:

$$\{\mathbf{P}\}_b = [\mathbf{B}]_b^t \{\mathbf{M}\}_b \tag{9}$$

4.3 Elasticity law: a relationship between generalized stress and deformation

The hypothesis of equivalence in deformations allows us to write the relationship between m_i, m_j, n and ϕ_i, ϕ_j, δ when there are local buckling and plastic rotations in the element (see Flórez-López *et al.* 2015). Now, the influence of corrosion is also included in the equation, in a simplified way, as follows:

$$\phi_i - \phi_i^p = \frac{L}{(1-d_i)3EI(c_i)} m_i - \frac{L}{6EI(c_j)} m_j$$
$$\phi_j - \phi_j^p = -\frac{L}{6EI} m_i + \frac{L}{(1-d_i)3EI(c_j)} m_j \tag{10}$$
$$\delta = \frac{L}{AE(c_i, c_j)} n$$

It can be observed that the damage state variables d_i and d_j characterize the degree of local buckling as related to the reduction of the element's stiffness. The terms ϕ_i^p ϕ_j^p are the permanent rotations remaining after an unloading process returns the bending moments to zero.

In addition, any of the phenomenological corrosion laws of section 2, or other similar ones complete this generalized elasticity law:

$$\dot{c}_i = F_{44}(c_i, p_{ci}, t); \quad \dot{c}_j = F_{55}(c_j, p_{cj}, t) \tag{11}$$

For instance, under fluvial conditions (see section 2.1, Eq. (2)), the generalized flexibility F_{44} can be given by:

$$F_{44} = \frac{a_2(p_{ci})}{th_0} \exp\left(\frac{a_1(p_{ci}) - c_i\, th_0}{a_2(p_{ci})}\right)$$
$$F_{44} = \bar{a}_2(p_{ci}) \exp\left(\frac{\bar{a}_1(p_{ci}) - c_i}{\bar{a}_2(p_{ci})}\right); \tag{12}$$
$$\bar{a}_1 = \frac{a_1}{th_0}; \quad \bar{a}_2 = \frac{a_2}{th_0}$$

where p_{ci} is, in this particular case, the flow velocity. In a step-by-step procedure, Eq (4) can be substituted by a finite difference approximation.

If instead the analysis needs to be carried out under marine conditions, (for instance, Eq. (4)), the generalized flexibility may be:

$$F_{44} = c_i B \left(\frac{c_i th_0}{A}\right)^{-\frac{1}{B}} = c_i B \left(\frac{c_i}{\bar{A}}\right)^{-\frac{1}{B}}; \quad \bar{A} = \frac{\bar{A}}{th_0} \tag{13}$$

4.4 Yield function and plastic evolution laws

Again, the hypothesis of equivalence in deformations allows to obtain a yield function, for a hinge i, with isotropic hardening considering the effect of local buckling. The yield (M_e) and ultimate (M_u) bending moments depend on the C/R variable and the axial force, thus:

$$f_i = \left|\frac{m_i}{1-d_i}\right| - M_e(c_i, n) - \left(M_u(c_i, n) - M_e(c_i, n)\right)\left(1 - e^{-\beta|\phi_i^p|}\right) \tag{14}$$

where β is a parameter related to the hardening rate of the hinge that is assumed to be a constant. The plastic hardening process has negligible influence on local buckling if the cross-section is compact. Then, if the goal is only collapsing analysis, this phenomenon can be neglected by making $\beta \to \infty$. In this case, the yield function becomes $f_i = \left|\frac{m_i}{1-d_i}\right| - M_u(c_i, n)$.

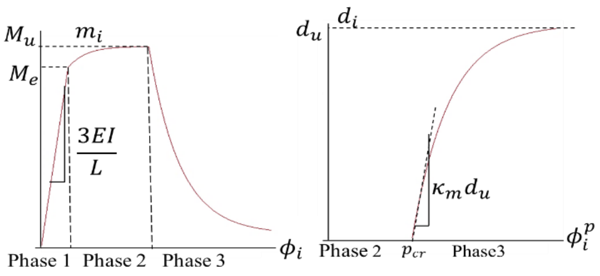

Fig. 5 Schematic representation of the LDM Parameters and their physical meaning

The plastic rotation evolution law can now be written as:

$$\begin{cases} \dot{\phi}_i^p = 0 \ \ if \ \ f_i < 0 \\ f_i = 0 \ \ if \ \ \dot{\phi}_i^p \neq 0 \end{cases} \tag{15}$$

4.5 Damage evolution law

An LB resistance function, $R(d_i)$ is also introduced as in (Febres *et al*. 2003):

$$R(d_i) = p_{cr}(c_i, n) - \frac{1}{\kappa_m(c_i, n)} \ln\left(1 - \frac{d_i}{d_u}\right) \tag{16}$$

where p_{cr} and k_m are now functions of the axial force and the C/R variable. The local buckling evolution law is now given by:

$$\begin{cases} \dot{d}_\iota = 0 \ \ if \ \ \left|\phi_i^p\right| < R(d_i) \\ \left|\phi_i^p\right| = R(d_i) \ \ if \ \ \dot{d}_\iota > 0 \end{cases} \tag{17}$$

The mechanical interpretation of the model's parameters, for constant corrosion and axial force, is shown in Fig. 5. Notice that d_u is the limit or ultimate value that the damage variable can assume, usually, equal to 0.9; p_{cr} represents the critical value of cumulated plasticity triggering LB; κ_m is related to the damage rate during the local buckling process. For small values of LB, the damage evolution law can be approximated to a straight line with a slope equal to $k_m d_u$.

5. Interaction diagrams

5.1 Interaction diagrams considering corrosion

In the model described in section 4, five functions $(EI(c_j), M_e(c_i,n), M_u(c_i,n), p_{cr}(c_i,n), \kappa_m(c_i,n))$ are assumed to be dependent on the corrosion state variable. As tubes come in pre-determined sizes, it is possible to obtain experimentally the interaction diagrams for all these parameters, as it will be shown in section 5.2

In the absence of that option, there are other possibilities. The first three variables can be computed using the standard techniques for determining the strength of materials, considering again that corrosion only reduces the thickness of the tube (as in George *et al*. 2021, George *et al*. 2022a, 2022b) and decreases the strength of the

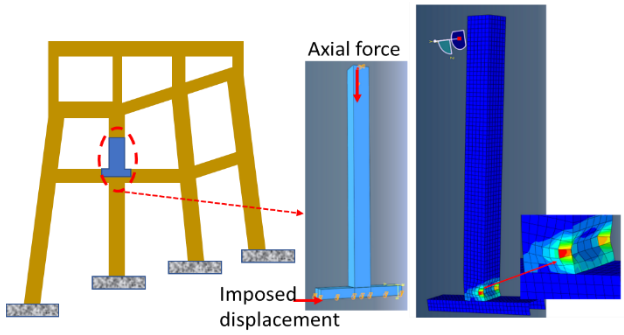

Fig. 6 Multi-scale approach, structure used for the computation of interaction diagrams

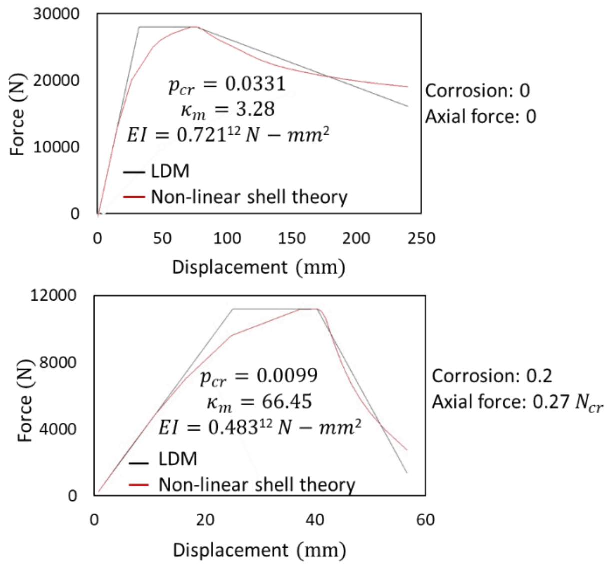

Fig. 7 Force vs. Displacement curves: Numerical Simulation vs. Reference Model

material. The last two can also be estimated by using any standard moment curvature relationship for tubes with local buckling, such as the classic ones described in (Inglessis *et al*. 1999), combined with some formulation for computing a plastic hinge length (Ribeiro *et al*. 2015, Zhou 2022, George *et al*. 2022b)

In this section, we explore a third alternative, the use of a multi-scale procedure where non-linear shell theory is only used to compute the interaction diagrams while the lumped damage model is the tool for the global analysis of the complex structure.

In order to obtain the interaction diagrams, a numerical specimen representing a beam column joint is represented in Fig. 6. The structure is subjected to an axial force distributed on the top of the specimen and perpendicular displacements.

Local buckling appears on the specimen close to the intersection between the two elements. Two forces vs. displacement curves obtained from this numerical analysis are shown in Fig. 7. The approximation using the lumped damage model is also included in the figure. From this estimate, it is possible to compute the values of the

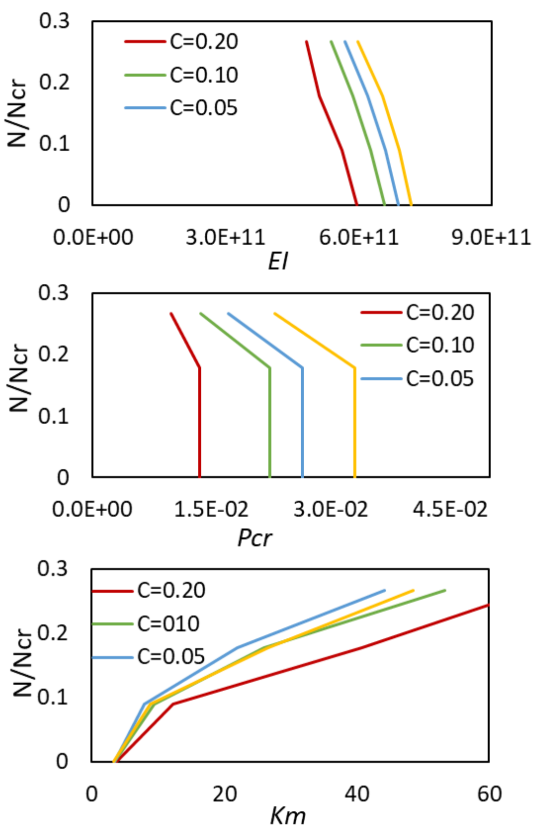

Fig. 8 Interaction Diagrams Showing the Influence of Corrosion on Key LDM Parameters

parameters of the model.

Repeating the process for a set of corrosion values and axial forces, it is possible to obtain the interaction diagrams presented in Fig. 8. On the vertical axes of those plots, the axial force is normalized with respect to the plastic axial force, i.e., the ultimate stress multiplied by the area of the cross-section. The values of $M_e(c_i, n)$ and $M_u(c_i, n)$ show good agreement with the strength of material values. Thus, it is not necessary to include their diagrams. It was found that the interaction diagrams show only a very weak dependence on the length of the elements. Thus, the same diagrams can be used in any structure using an element with the same cross-section. However, in the case of applications with radically different lengths, it may be convenient to check their validity.

5.2 Interaction diagrams considering corrosion

Corrosion reduces the values of the yield and ultimate moments M_e, M_u, the bending stiffness EI and the critical plastic rotation p_{cr} while increasing the rate parameter κ_m. During a process of repair, the opposite effects are observed.

George *et al*. (2022) investigated the evolution of the local buckling strength of steel tubular members subjected to mechanical or chemical corrosion and then repaired using Carbon Fiber Reinforced Polymers (CFRP). The tests were carried out in 4-point bending specimens. Fig. 9 compares the performance of several specimens that were corroded or

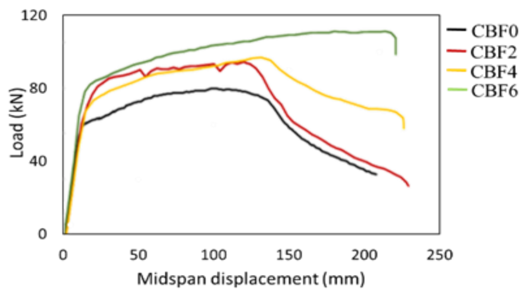

Fig. 9 Force vs Displacement curves under varying Repair conditions by George *et al*. (2022b)

corroded and then repaired. The curve labeled CBF0 corresponds to the specimen corroded ($c = 0.2$) but not repaired; CBF2W represents the behavior of an element corroded and then repaired using 2 layers of CFRP and so on.

Using the model of section 4, these tests can be characterized with the structure shown in Fig. 10a. Only half of the specimen is represented using a mesh of two elements and three nodes. The following boundary conditions are considered: $u_1 = w_1 = 0 = c_1 = c_2 = \theta_3 = 0$. The loading consists of a vertical displacement-controlled force on the node 2 ($w_2 = w_2(t)$) and a corrosion-controlled process on node 3 ($c_3 = c_3(t)$). These loading histories are represented in the Fig. 10(b). The first step represents the corrosion phase. The second one corresponds to a period of repair, I.e., a stage of negative corrosion increments. In the third and last step, the mechanical loading is incremented until local buckling appears in the structure.

Notice that the ultimate moment M_u can be computed as the maximum force in Fig. 10 times $L_1/2$, where L_1 is the length of the first element. An equivalent corrosion increment can then be computed as the necessary value of the tube thickness to obtain the experimentally identified M_u with an ultimate stress ($\sigma_u = 543\ kN/mm^2$): $\Delta c = 0$ for the test CBF0, $\Delta c = -0.05$ for CBF2W, $\Delta c = -0.065$ for CBF4W, and $\Delta c = -0.13$ for CBF6W. A simulation of these tests, neglecting the plastic hardening phase, is presented in Fig. 11. The numerical results are labeled as UEL-CBF0, UEL-CBF2 and so on. From these numerical results, it is possible to obtain some points of an interaction diagram for repair as presented in Fig. 12.

During a repairing step, i.e., with negative increments of corrosion, the values p_{cr} increase and those of κ_m decrease as observed in Figs. 11 and 12. Both interaction diagrams, corrosion and repair can be included in the analysis.

Again, in the absence of experimental results, the interaction diagrams for repair can also be obtained numerically by the same multi-scale procedure described in section 5.1. Kabir *et al.* (2016) reported that using conventional shell elements from commercial FE programs, it is possible to reproduce the experimental behavior of repaired tubular elements.

Although the current study focused on CFRP-based repairs, the proposed modeling framework is general and can accommodate other repair techniques, such as steel

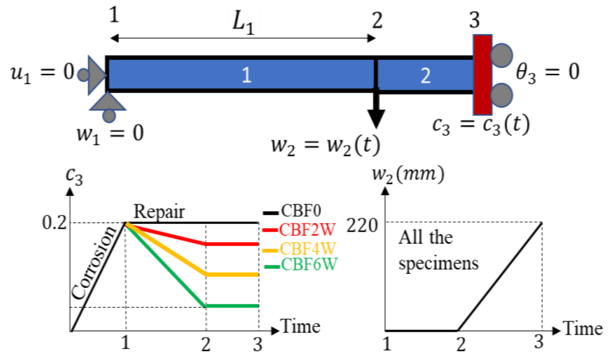

Fig. 10 Analytical modeling of the repair. Corrosion history and displacement-controlled force history

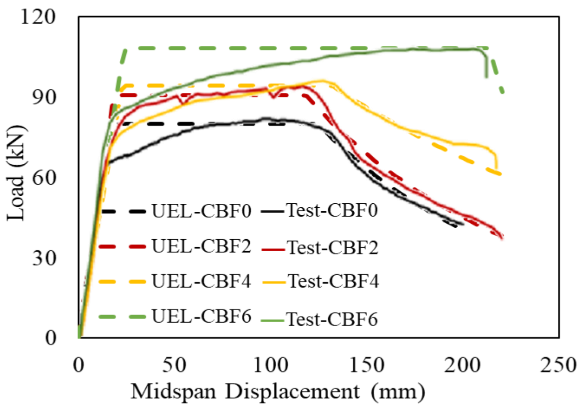

Fig. 11 Force vs. displacement, comparison between model and tests by (J. M. George, y otros 2022)

jacketing, epoxy injection, or bolted reinforcements, provided that their mechanical effects (on stiffness and strength) can be captured through modified interaction diagrams or equivalent damage reductions.

6. Numerical simulation of the tubular steel frame

The models proposed in sections 4 and 7 were implemented in a commercial finite element program (Simulia 2017) as a user element. In this section, the results of a simulation of the test described in section 3.3 are presented. The frame was modeled using a mesh with only 6 nodes and elements, as shown in Fig. 13. The ultimate and yield moments were computed using the conventional procedures with a yield stress equal to $550\ MPa$; the other parameters were obtained from the interaction diagrams of Fig. 8. The first plastic hardening stage was again neglected. The corrosion variables were imposed equal to zero in all the nodes of the frame. Nodes 1 and 4 are completely fixed, and mono-sign displacement histories are applied to nodes 2 and 3.

The curves of force vs. displacement obtained in the simulation are compared with the experimental ones in Fig. 13(a). Finally, Fig. 13(b) shows the damage map at the end of the simulation. Notice the reasonably good agreement with the experimental results. It can also be pointed out that,

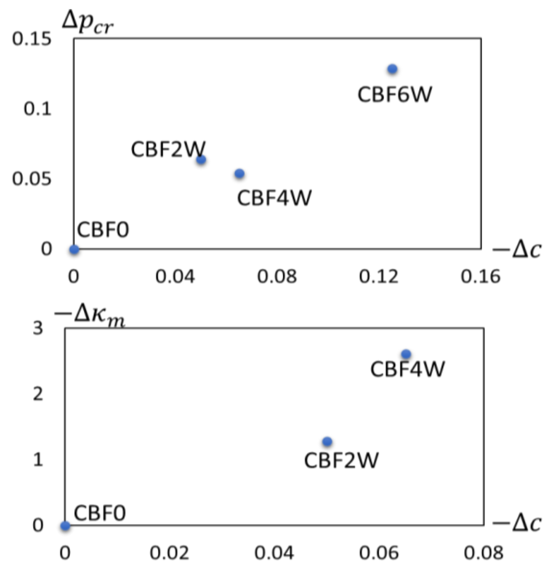

Fig. 12 Interaction diagram of p_{cr} and κ_m for repairing

at least from a qualitative point of view, this damage map represents the local buckling locations and intensities observed in the test.

7. Modeling of local buckling for cyclic loading

The model of section 5 can be generalized to the case of cyclic loadings. The elasticity law under cyclic loading and assuming unilaterality of the behavior is now given by the following expression:

$$\phi_i - \phi_i^p = \frac{L}{(1-d_i^+)3EI(c_i)}\langle m_i\rangle_+ + \frac{L}{(1-d_i^-)3EI(c_i)}\langle m_i\rangle_- - \frac{L}{6EI(c_j)}m_j$$

$$\phi_j - \phi_j^p = -\frac{L}{6EI}m_i + \frac{L}{(1-d_j^+)3EI(c_j)}\langle m_j\rangle_+ + \frac{L}{(1-d_j^-)3EI(c_j)}\langle m_j\rangle_- \quad (18)$$

$$\delta = \frac{L}{AE(c_i,c_j)}n$$

where $\langle m\rangle_+$ represents the positive part of m ($\langle m\rangle_+ = m\ if\ m > 0;\ \langle m\rangle_+ = 0\ otherwise$) $\langle m\rangle_-$ is the negative part of m ($\langle m\rangle_- = m\ if\ m < 0;\ \langle m\rangle_- = 0\ otherwise$) With the same corrosion evolution law of the mono-sign case (8).

Notice that now there are two damage variables. The first one (d_i^+) quantifies the degree of local buckling due to positive bending moments on the element; the other one (d_i^-) characterizes local buckling due to negative bending moments (see Fig. 2(a)).

Neglecting plastic hardening again, the yield function is:

$$f_i = Max\begin{cases} m_i - (1-d_i^+)M_u(c_i,n) \\ -m_i + (1-d_i^-)M_u(c_i,n) \end{cases} \quad (19)$$

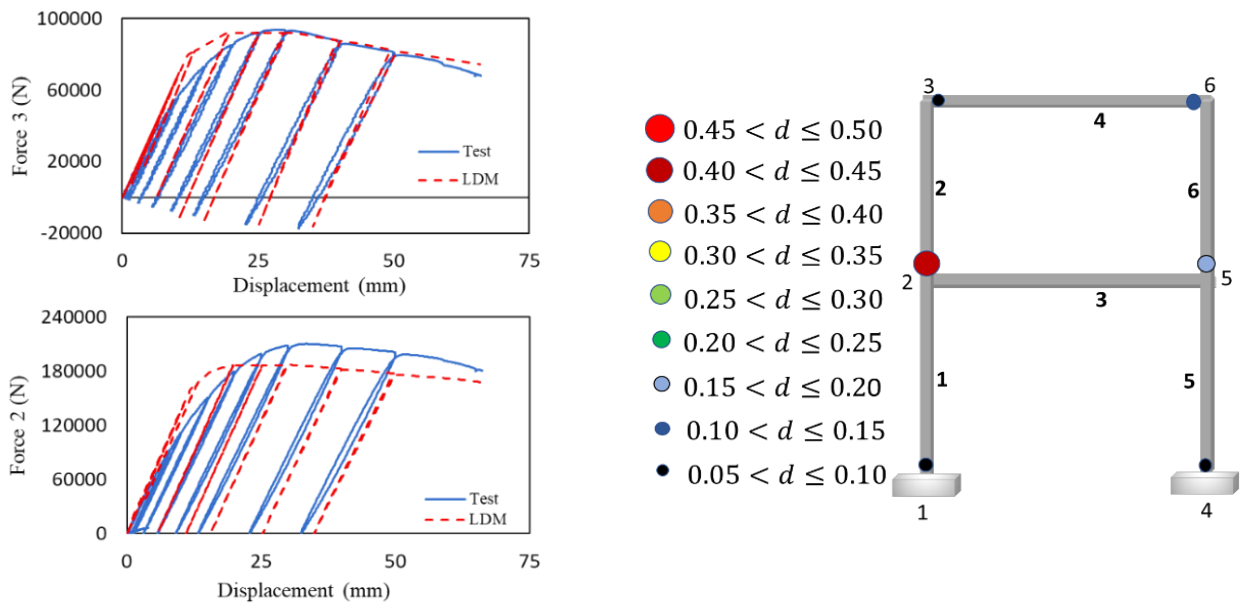

(a) Force vs. displacement at nodes 2 and 3 (b) Damage map

Fig. 13 LB map at the end of the simulation

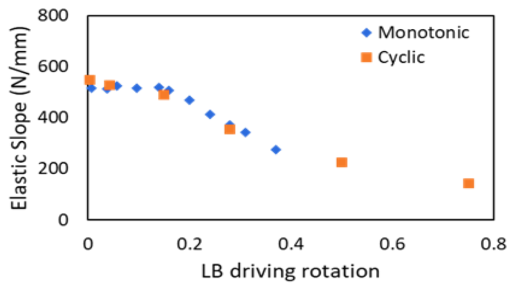

Fig. 14 Numerical simulation of a cyclic test, slope of the positive unloading against LB driving rotation

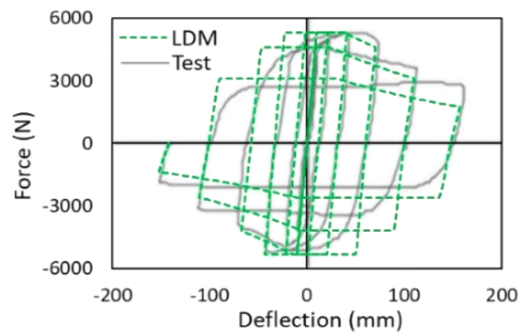

Fig. 15 Numerical simulation of a cyclic test, Force vs. deflection response

Fig. 2(b) showed that plastic rotation or even the cumulated plastic rotation cannot be used as a local buckling driving variable due to the counter-buckling effect described in section 3.2.

Therefore, new variables, the damage driving rotations b_i^+, b_i^-, are introduced:

$$\dot{b}_i^+ = \langle \dot{\phi}_i^p \rangle_+ + 0.6 \langle \dot{\phi}_i^p \rangle_- \\ \dot{b}_i^- = -\langle \dot{\phi}_i^p \rangle_- - 0.6 \langle \dot{\phi}_i^p \rangle_+ \tag{20}$$

For a positive LB phase (wrinkling phase) $\dot{b}_i^+$ increases while, after a change of sign of the loading (ironing phase), this variable decreases by a factor 0.6. This number is experimentally identified as shown in Fig. 14.

Notice that in a monotonic loading, this variable is equal to the absolute value of the plastic rotation; for cyclic loadings, the new driving rotation considers counter-buckling. The LB evolution laws are now:

$$\begin{cases} \dot{d}_i^+ = 0 \quad if \quad b_i^+ < R(d_i^+) \\ b_i^+ = R(d_i^+) \; if \quad \dot{d}_i^+ > 0 \end{cases} \\ \begin{cases} \dot{d}_i^- = 0 \quad if \quad b_i^- < R(d_i^-) \\ b_i^- = R(d_i^-) \; if \quad \dot{d}_i^- > 0 \end{cases} \tag{21}$$

where the function $R(d_i^{+/-})$ is the same that was introduced in section 4.5. Therefore, in order to initiate local buckling, the driving rotation must reach the value p_{cr}. For an easier interpretation of the plasticity maps, a normalized damage driving rotation as follows: $ddr = Max\left(\frac{b_i^+}{p_{cr}}, \frac{b_i^-}{p_{cr}}\right)$. Thus, for $ddr = 1$, local buckling appears in at least one of the hinges' sides (Fig. 16).

The test described in section 3.2 (Fig. 15a), was simulated with the constitutive model described in this section with the following parameters: $\sigma_u = 300\, MPa$, $EI = 2.06e10\; N - mm^2$, $\kappa_m = 2.2$, $p_{cr} = 0.13$; plastic hardening was again neglected.

8. Parametric examples

8.1 Influence of corrosion time on the earthquake resistance of a river structure

In this section, a parametric analysis carried out on the structure of Fig. 17 is described. The tubes of the frame

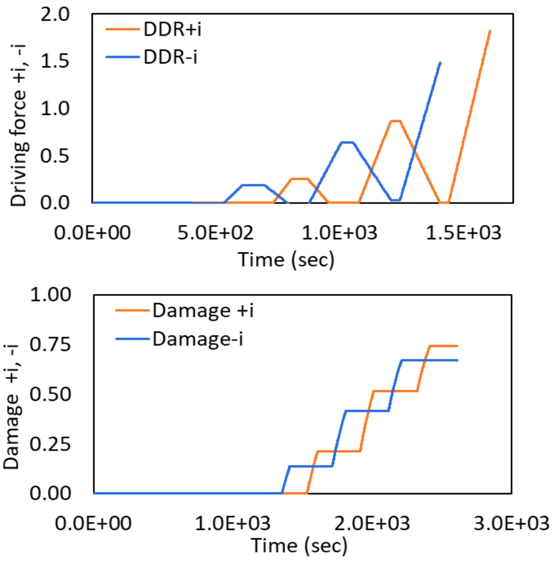

Fig. 16 ddr evolution and damage evolutions

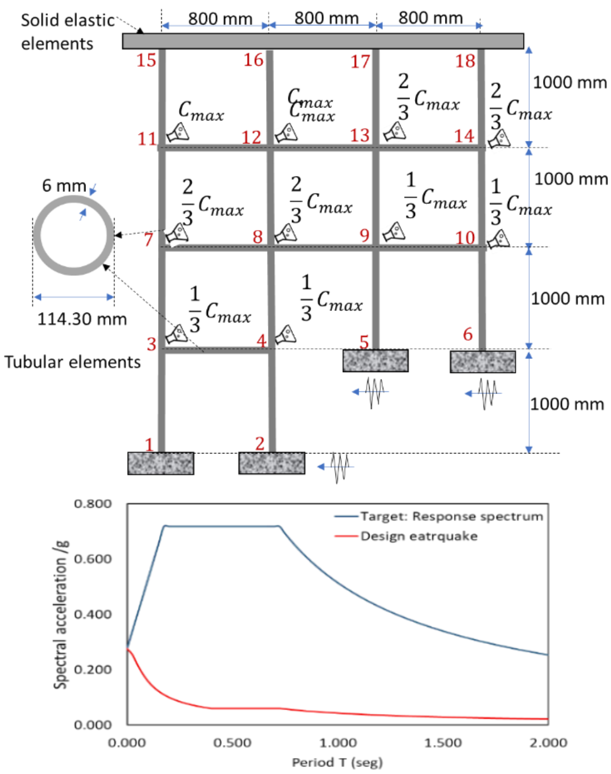

Fig. 17 Wharf bridge frame subjected to corrosion and earthquake loadings

have the same cross-section as the experimental tests described in section 5.2

This construction is representative of a frame-type wharf. The first step in all simulations corresponds to the application of vertically distributed loads on the elastic elements at the top of the frame. The second step corresponds to corrosion-controlled loads (except in the reference frame with zero corrosion) on nodes 3–4, 7–14. It is assumed that the corrosion distribution is proportional to the height of the node. In the reference simulation, an

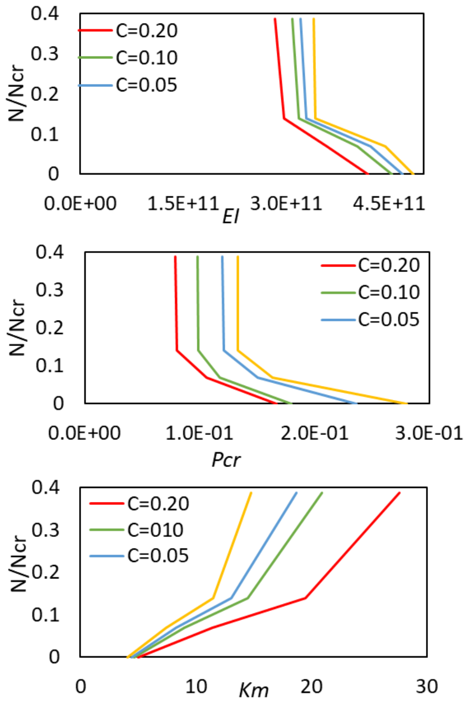

Fig. 18 Interaction diagrams of corrosion effects

earthquake loading is applied to the uncorroded structure. The acceleration record was artificially generated from the spectrum shown in the same figure

The interaction diagrams were computed numerically with the procedure described in section 5.1 and are indicated in Fig. 18. Equivalent mass values were added to the elastic elements of the top of the frame, representing the contribution of the platform and its equipment.

No local buckling appeared in the frame, and low values of permanent rotations were generated, as shown in the map of ddr at the end of event presented in Fig. 19. Notice that the maximum value of $ddr = 0.4$ appeared on node 5 of the frame.

In the remaining simulations, the structure was first subjected to chemical forces so that maximum corrosion values of 0.05, 0.1, 0.15 and 0.2 are reached Fig. 20. At the end of each corrosion steps, the same earthquake loading was applied to the structure.

Notice that, as corrosion is zero at the bottom of the columns, local buckling finally appeared for a maximum corrosion of 0.2 in a hinge adjacent to node 14. These analyses can help establish limit values for corrosion that may endanger the safety of the structure. Defining limit values of ddr for some representative loads may be used to decide when major maintenance processes are needed in critical structures. Then the same FE can be used for the design and/or evaluation of retrofitting projects, as presented in the next example.

8.2 Evaluation of a retrofitting project after long-term exposure

In the example of this section, the same structure with a maximum corrosion state of 0.2 as the previous one is

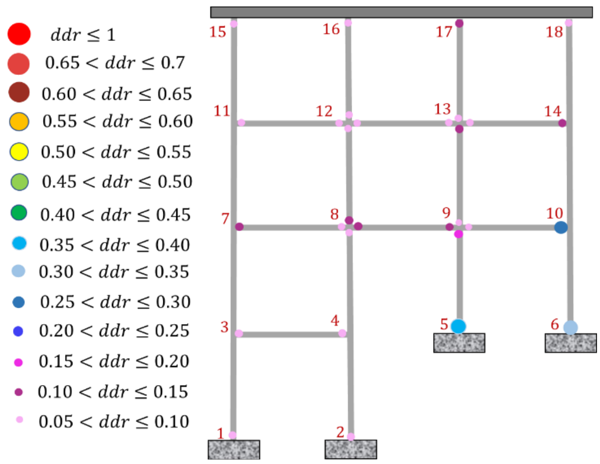

Fig. 19 Map of ddr at the end of the earthquake for the uncorroded wharf frame

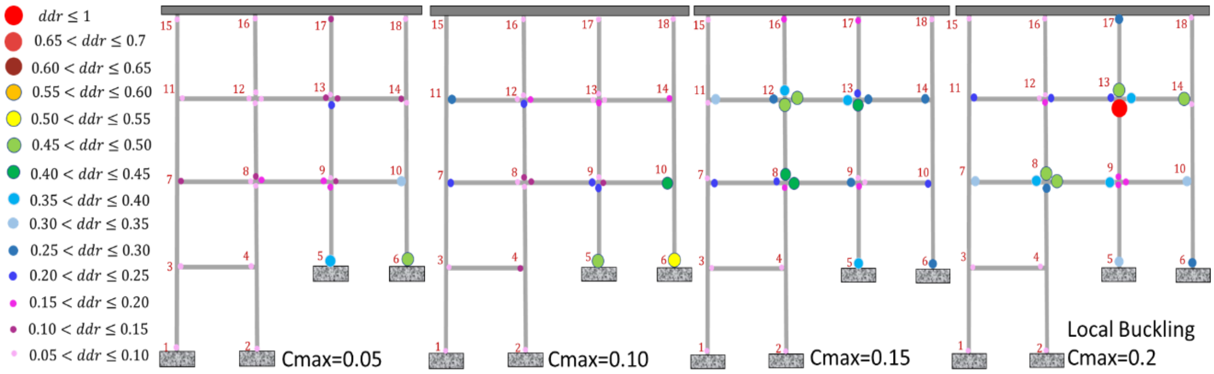

Fig. 20 Maps of ddr after four corrosion stages under the same earthquake loading

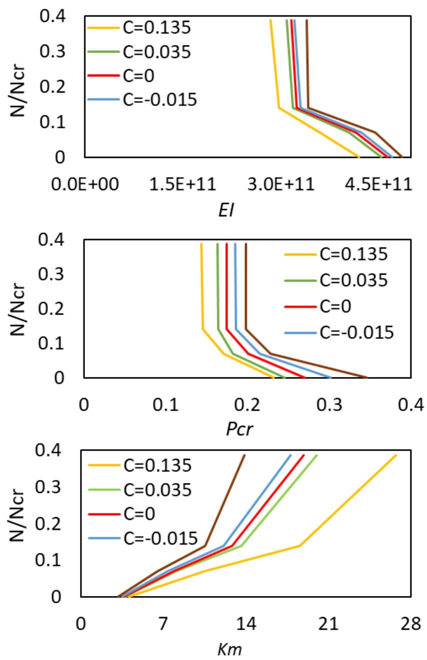

Fig. 21 Interaction diagrams of repair

considered. As aforementioned, the reference earthquake loading would produce a severe damage state that would even trigger local buckling. Therefore, retrofitting projects using the technique described in section 5.2 are considered preemptive measures

Three different retrofitted structures with 2, 4, and 6 bands on the joints of the frame are analyzed. The goal of these analyses is to evaluate the reduction of expected ddr values in the case of the seismic event described in section 8.1.

In the input file of the FE analysis, the process is represented in three steps. In the first one, the vertical loads corresponding to the loads on the upper platform are applied. In the second step, corrosion-controlled chemical forces are applied, as in the previous example. Then, the structure is retrofitted; this is characterized by imposing negative increments of corrosion on all the nodes of the frame; for the repair project with two bands, the corrosion increment is, as indicated in section 5.2, equal to -0.05; in the case of 4-band and 6-band repairs, the increments are respectively, -0.065 and -0.13. In the last step, seismic horizontal accelerations are imposed of the supports on the frame.

Numerically, the effect of the retrofitting is modeled using repair interaction diagrams as described in section 5.2 (Fig. 19). In this academic example, numerical ones, updated considering the experimental results, were used for the simulation and are represented in Fig. 22.

Notice that the three options avoid the severe damage state by the corroded frame. In the case of 6-band

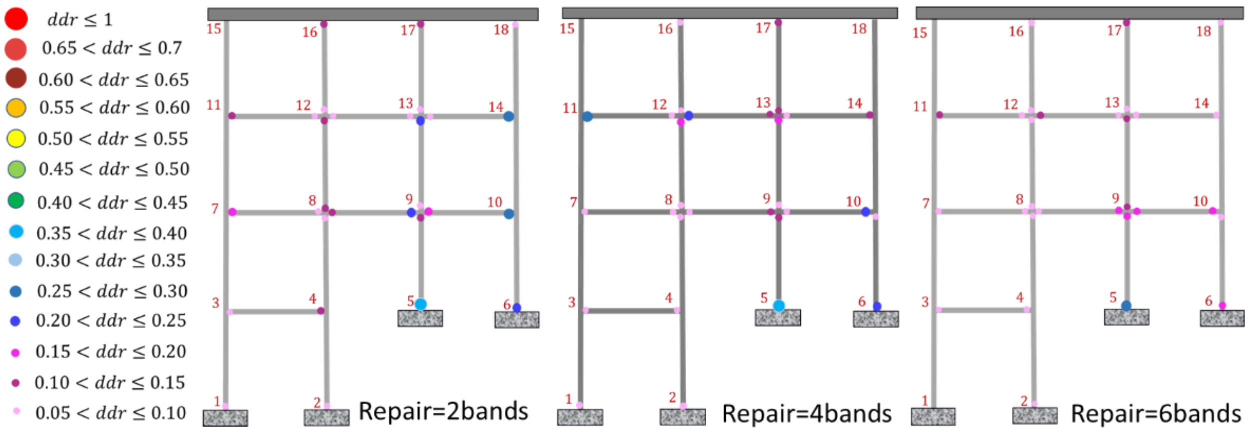

Fig. 22 Distribution maps of ddr after seismic loads are applied on the retrofitted frame

retrofitting, the structure is expected to have even better behavior than the original one.

5. Conclusions

In this paper, a new procedure and computational tool for the evaluation of complex tubular structures in corroded environments have been proposed. The data for the LDM analysis can be obtained from experimental results, non-linear shell analysis, or a combination of both in a multi-scale process. In this sense this LDM approach can be seen, both, as an alternative and as a complement to conventional procedures such as nonlinear shell theories.

Although probabilistic aspects were not addressed in this work, they clearly represent a fundamental part of the problem. Key components of the phenomena, corrosion progression, repair effectiveness, and the nature and intensity of occasional overloads, are inherently random. The mathematical model and FE formulation proposed here were conceived for use in probabilistic or stochastic analyses. While conventional FE with shell elements may capture the C/R process more accurately than LDM, its computational cost quickly becomes prohibitive for complex structures. In contrast, LDM enables the integration of more refined probabilistic procedures, yielding predictions of higher quality by combining simpler analyses with advanced stochastic methods. Even more importantly, the results of shell analysis consist mainly of color maps and deformed configurations.

From these, local buckling happenstance or its proximity can be inferred visually, but during probabilistic analyses, these characteristics should be determined automatically. This process can be carried out by considering damage indexes computed by postprocessors or even more complex procedures. But, if that is the case, it does not seem really useful to compute computationally expensive massive data that will never be used, only the global indexes. Again, the internal variables computed in the LDM analysis, such as local buckling driving rotations or state damage variables are certainly more accurate indicators of the global state of deterioration or the efficacy of retrofitting than any postprocessor index. Another important advantage of the proposed procedure consists in carrying out sequential analyses when corrosion is followed by retrofitting processes and finally mechanical loadings of any nature since the effects of C/R progressions are modeled via their influence on the behavior in a single input file, while the shell alternative needs remeshing for the same purposes.

References

Aksoylu, C., Ozkilic, Y.O., Yazman, S., Alsdudi, M., Gemi, L. and Arslan, M. H. (2023), "Numerical and analytical investigation of parameters influencing the behavior of shear beams strengthened by CFRP wrapping", *Steel Compos. Struct.*, **47**(2), 217-238. https://doi.org/10.12989/SCS.2023.47.2.217.

Bambach, M.R. and Elchalakani, M. (2007), "Plastic mechanism analysis of steel SHS strengthened with CFRP under large axial deformation", *Thin-Wall. Struct.*, **45**, 159-170. https://doi.org/10.1016/j.tws.2007.02.004.

Bambach, M.R., Elchalakani, M. and Zhao, X.L. (2009), "Composite steel–CFRP SHS tubes under axial impact", *Compos. Struct.*, **87**(3), 282-292. https://doi.org/10.1016/j.compstruct.2008.02.008.

Chakrabarty, J. (2006), *Theory of Plasticity. Pensilvania, United State*, https://doi.org/10.1016/C2009-0-05774-2.

Coelho, K., Leonel, E. and Flórez-López, J. (2019), "An efficient mechanical-probabilistic approach for the collapse modelling of RC structures", *Ibracom Struct. Mater. J.*, **12**(2), 386-397. https://doi.org/10.12989/cac.2022.29.1.001.

Coelho, K., Leonel, E. and Julio Flórez-López. (2022), "A methodology to evaluate corroded RC structures using a probabilistic damage approach", *Comput. Concrete*, **29**(1), 1-14. http://dx.doi.org/10.1590/S1983-41952019000200010.

Di Sarno, L., Majidian, A. and Karagiannakis, G. (2021), "The effect of atmospheric corrosion on steel structures", *Buildings*, **11**, 1-19. https://doi.org/10.3390/buildings11120571.

Djeddi, L. and Abdelaziz A. (2020), "Corrosion initiation time models in RC coastal structures based on reliability approach", *Adv. Concrete Construct.*, **9**(2), 148-159. https://doi.org/10.12989/ACC.2020.9.2.149.

Elchalakani, M. (2014), "Plastic collapse analysis of CFRP strengthened and rehabilitated degraded steel welded RHS beams subjected to combined bending and bearing", *Thin-Wall. Struct.*, **82**, 278-295. http://dx.doi.org/10.1016/j.tws.2014.05.002.

Elchalakani, M. and Fernando, D. (2012), "Plastic mechanism analysis of unstiffened steel I-section beams strengthened with CFRP under 3-point bending", *Thin-Wall. Struct.*, **53**, 58-71. https://doi.org/10.1016/j.tws.2012.01.005.

Elchalakani, M., Karrech A., Basarir H., Hassanein M. and Fawzia S. (2017), "CFRP strengthening and rehabilitation of corroded steel pipelines under direct indentation", *Thin-Wall. Struct.*, **119**, 510-521. https://doi.org/10.1016/j.tws.2017.06.013.

Elchalakani, M., Karrech A., Basarir H., Zhao, X.-L., Fawzia, S. and Hassanein, M.F. (2017), "Strengthening of mild steel struts using CFRP sheets subjected to uniform axial compression", Thin-Wall. Struct., **166**, 96-112. https://doi.org/10.1016/j.tws.2017.03.010.

Febres, R., Inglessis P. and Flórez-López J. (2003), "Modeling of local buckling in tubular steel frames subjected to cyclic loading", *Comput. Struct.*, **81**, 2237-2247. https://doi.org/10.1016/S0045-7949(03)00292-X.

Flórez-López, J. (1999), *Plasticidad y fractura en estructuras aporticadas. Madrid, Spain: A. H. Barbat. Monografía CIMNE IS-35*, Universidad Politecnica de Madrid. ISBN: 84-89925-46-1

Flórez-López, J., Picón, R. and Marante, M. (2015), *Fracture and Damage Mechanics for Structural Engineering of Frames: State-of-the-Art Industrial*, Hershey PA, United States of America: IGI Global. https://doi.org/10.4018/978-1-4666-6379-4.

George, J., Kimiaei M., Efthymiou M. and Elchalakani M. (2022b). "Flexural response of underwater offshore structural members retrofitted with CFRP wraps and their performance after exposure to real marine conditions", *Structures*, **43**, 559-573. https://doi.org/10.1016/j.istruc.2022.06.075.

George, J., Kimiaei M., Elchalakani M. and Fawzia S. (2021), "Experimental and numerical investigation of underwater composite repair with fiber reinforced polymers in corroded tubular offshore structural members under concentric and eccentric axial loads", *Eng. Struct.*, **227**, 111402. https://doi.org/10.1016/j.engstruct.2020.111402.

George, J., Kimiaei M., Elchalakani M. and Fawzia S. (2022a), "Underwater strengthening and repairing of tubular offshore structural members using Carbon Fibre Reinforced Polymers with different consolidation methods", *Thin-Wall. Struct.*, **174**, 109090. https://doi.org/10.1016/j.tws.2022.109090.

Hamzeh, K. (2017), "Numerical investigation on the behavior of SHS steel frames strengthened using CFRP", *Steel Compos. Struct.*, **24**(5), 561-568. https://doi.org/10.12989/SCS.2017.24.5.561.

Inglessis, P., Gomez, G., Quintero, G. and Flórez-López J. (1999), "Model of damage for steel frame members", *Eng. Struct.*, **21**(10), 954-964. https://doi.org/10.1016/S0141-0296(98)00038-8.

Inglessis, P., Medina S., López, A., Febres, R. and Flórez-López J. (2002), "Modeling of local buckling in tubular steel frames by using plastic hinges with damage", *Steel Compos. Struct.*, **2**(1), 21-34. https://doi.org/10.1201/9781003211198-5.

ISO-9223, International Standard. (2012), *Corrosion of Metals and Alloys—Corrosivity of Atmospheres—Classification, Determination and Estimation. International Standard*, Geneva, Switzerland: Technical Committee ISO/TC 156.

ISO-9224, International Standard. (2012), *Corrosion of Metals and Alloys–Corrosivity of Atmospheres–Classification, Determination and Estimation. International Standard*, Geneva, Switzerland: Technical Committee ISO/TC 156.

ISO-9226, International Standard. (2012), *Corrosion of metals and alloys — Corrosivity of atmospheres —Determination of corrosion rate of standard specimens for the evaluation of corrosivity. International Standard*, Geneva, Switzerland: Technical Committee ISO/TC 156.

Jabed, A., Tusher M., Shuvo Md. and Imam A. (2023), "Corrosion of steel rebar in concrete: A review", *Corrosion Sci. Technol*., **22**(4), 273-286. https://doi.org/10.14773/CST.2023.22.4.273.

Kabir, M., Fawzia S., Chan, T.H., Gamage, J.C., Bai, J.B. (2016). "Experimental and numerical investigation of the behaviour of CFRP strengthened CHS beams subjected to bending", *Eng. Struct*., **113**, 160-173. https://doi.org/10.1016/j.engstruct.2016.01.047.

Kabir, M., Fawzia, S. and Chan T.H. (2015). "Effects of layer orientation of CFRP strengthened hollow steel members." Graevinar, **67**, 441-451. https://doi.org/10.14256/JCE.1127.2014.

Kim, J. and Noh H.-C. (2012), "Design optimization of blast resistant CFRP-steel composite structure based on reliability analysis", *J. Korean Soc. Adv. Compos. Struct*., **3**(4), 10-16. https://doi.org/10.11004/kosacs.2012.3.4.010.

Klinesmith, D.E., McCuen, R.H. and Albrecht, P. (2007), "Effect of environmental conditions on corrosion rates", J. Mater. Civil Eng., **19**(2), 121-129. https://doi.org/10.1061/(ASCE)0899-1561(2007)19:2(121).

Lee, S.J., Han, M.S., Jang, S.K. and Kim, S.J. (2015), "Effect of flow velocity on corrosion rate and corrosion protection current of marine material", Corrosion Sci. Technol., **14**(5), 226-231. https://doi.org/10.14773/CST.2015.14.5.226.

Liu, M., Zeng, L., Wu, L. and Zhu, C. (2022), "Effect of periodic water-sedimentation laden flow on damage for steel piles", *Front. Environ. Sci*., 1-12. https://doi.org/10.3389/fenvs.2022.971786.

Meiling, C. and Sreekanta, D. (2009), "Experimental study on repair of corroded steel beam using CFRP", *Steel Compos. Struct*., **9**(2), 103-118. https://doi.org/10.12989/SCS.2009.9.2.103.

Momber, A. (2011), "Corrosion and corrosion protection of support structures for offshore wind energy devices (OWEA)", *Mater. Corrosion*, **62**, 391-404. https://doi.org/10.1002/maco.201005691.

Palanisamy, R., Jung, B.-J., Sim, S.-H. and Yi, J.-H. (2019), "Quasi real-time and continuous non-stationary strain estimation in bottom-fixed offshore structures by multimetric data fusion", *Smart Struct. Syst*., **23**(1), 61-69. https://doi.org/10.12989/SSS.2019.23.1.061.

Rahgozar, R., Sharifi, Y. and Malekinejad, M. (2010), "Buckling capacity of uniformly corroded steel members in terms of exposure time", *Steel Compos. Struct*., **10**(6), 475-487. https://doi.org/10.12989/SCS.2010.10.6.475.

Ribeiro, F., Barbosa, A., Scott, M. and Neves, L. (2015), "Deterioration modeling of steel moment resisting frames using finite-length plastic hinge force-based beam-column elements", *Struct. Eng*., **141**(2), 1-12. https://doi.org/10.1061/(ASCE)ST.1943-541X.0001052.

Sbhal, I. and Chen, W. (1984), "Moment–curvature expressions for fabricated tubes", *J. Struct. Eng*., **110** (11), 2738-2757. https://doi.org/10.1061/(ASCE)0733-9445(1984)110:11(2738).

Shi, W., Tong, L., Chen, Y., Li, Z. and Shen, K. (2012), "Experimental study on influence of corrosion on behavior of steel material and steel beams", *J. Build. Struct*., **33**(7), 53-60.

Shigenobu K., Yamamoto, Y., Ahn, J.H. and Jeong Y.-S. (2018), "Evaluation method for time-dependent corrosion depth of uncoated weathering steel using thickness of corrosion product layer", *Struct. Eng. Mech*., **65**(2), 191-201. https://doi.org/10.12989/SEM.2018.65.2.191.

Simulia. (2017), *Abaqus/Cae [Computer software]*. Dassault Systèmes, Paris France.

Uriayer, F.A. and Alam, M. (2013), "Mechanical properties of steel-CFRP composite specimen under uniaxial tension", *Steel Compos. Struct*., **15**(6), 659-677. https://doi.org/10.12989/SCS.2013.15.6.659.

Zhou, Y., Ning, S., Huang, D. and Li, Y. (2022), "Refined plastic hinge method for steel frames with local–global interactive buckling", *Thin-Wall. Struct*., **181**, 110013. https://doi.org/10.1016/j.tws.2022.110013.